Evaluation and Realization of Safer Mg-S Battery: the Decisive Role of the Electrolyte

Lin Sheng[‡a], Zhangxiang Hao[‡a], Junrun Feng[a], Wenjia Du[c], Manxi Gong[a], Liqun Kang[a], Paul R. Shearing[c,d], Dan J. L. Brett[c], Yunhui Huang,[b,*] Feng Ryan Wang[a,*]

[a] Materials and Catalysis Laboratory, Department of Chemical Engineering, University College London, Roberts Building, Torrington Place, London WC1E 7JE, UK

[b] State Key Laboratory of Materials Processing and Die & Mould Technology, School of Materials Science and Engineering, Huazhong University of Science and Technology, Wuhan 430074, China.

[c] Electrochemical Innovation Lab, Department of Chemical Engineering, University College London, Roberts Building, Torrington Place, London WC1E 7JE, UK

[d] Harwell Sci & Innovat Campus, Faraday Institution, Didcot OX11 0RA, Oxon, England

E-mail: huangyh@hust.edu.cn (Y. H. Huang), ryan.wang@ucl.ac.uk (F. R. Wang)

‡ These authors contributed equally to this work.

The magnesium–sulfur (Mg-S) battery may be a safer alternative for the lithium-sulfur battery because Mg plating usually proceeds without dendrite formation. Here, we correlate the thermal runaway of Mg-S battery with the associated change of electrolyte vapour pressure *via* battery testing calorimetery. Over-pressure builds up along with the programmed heating of the cell, and as a result, the thermal runaway is triggered at 20 to 45 K over the electrolyte boiling point, corresponding to 70 to 150 kPa pressure difference between the cell and the environment. The distinct performance-safety-cost behaviours of three ether type of electrolytes stems from the different CH_2CH_2O chain lengths. Such molecular insight will serve as a fundamental guideline in choosing and designing the desired electrolyte that simultaneously achieves a high explosion limit and good electrochemical performance.

Efficient and reversible energy storage is a driving force to enable consumer electronics, automotive propulsion, and to solve the intermittency of green electricity generation [1–5]. For domestic applications, a key requirement is to safely charge and discharge the battery at high energy densities [6,7]. One strategy to achieve high energy density is *via* the use of a Li-metal anode due to its specific capacity and low potential [8,9]. Upon cycling, metallic lithium forms needle-like dendrites, which impedes electrochemical performance over time and poses a fire hazard due to short circuit [10,11].

The magnesium-sulfur (Mg-S) battery is proposed to mitigate this safety concern as the production of magnesium dendrites is only seen at extreme condition with current density above 0.3 mA cm^{-2} [11–17]. Mg also has a high flash point, which is generally beyond the initial thermal runaway temperature of the battery. In addition, Mg is the fifth abundant element in the earth's crust [11,18], with a price 1/24 to that of lithium [19], and has a potential of -2.37 V relative to SHE. The divalent Mg^{2+} enables two electrons transfer per Mg atom, providing a theoretical specific mass capacity of 2,205 mAh g^{-1} and a specific volume capacity of 3,832 mAh cm^{-3} [20–23]. While Mg-metal anode does not pose a potential risk due to the plating/stripping process [24–26], the thermal stability of the organic electrolytes that are employed in the Mg-S battery are a safety bottleneck of the whole system. So far, the thermal stability of the organic electrolytes and their safety concerns during battery operation are largely unknown [27–34]. A systematic methodology is required to perform battery safety evaluations and to identify the key descriptor to understand the physical and chemical changes of the electrolyte during thermal runaway [35–38]. Researchers have realized the importance of battery thermal safety and have carried out research, Xu et al. reported on the multi-level thermal safety of lithium batteries [39].

Here we evaluate the safety of three electrolytes by testing the Mg-S battery response to a controlled failure scenario, they are: 1,2-dimethoxyethane (DME), diglyme (DEG) and tetraglyme (TEG). The DME cell explodes at 403 ± 4 K (45 K above the boiling point) with

2

corresponding vapour pressure of 249 ± 14 kPa. The DEG cell explodes at 455 ± 6 K (20 K above the boiling point) with corresponding vapour pressure of 172 ± 28 kPa. TEG has a higher boiling point, and thus the cell does not explode within the temperature range of the test. The result shows that the thermal runaway of the Mg-S batteries studied here is caused by the *in situ* heating and vaporization of the electrolyte, while the Mg anode and S cathode stay completely intact. Therefore, the vapour pressure of the electrolyte is the key descriptor of the overall battery safety. This conclusion suggests a potential way of optimizing battery safety and performance by molecular engineering new electrolyte systems with high ion conductivity and low vapour pressure.

The overall evaluation of a battery electrolyte contains three criteria: electrochemical performance, safety, and cost (**Figure 1**a). To study the electrolyte safety, the typical battery thermal runaway process needs to be simulated. It usually contains three stages [31]: 1: The onset of overheating in which the batteries arrive in an abnormal state with an increase of internal temperature; 2: Gasification of the electrolyte as the result of the heat accumulation. 3: Combustion and explosion of flammable electrolytes. To simulate this process, a programmed temperature profile is applied to the Mg-S coin cell at a given heating rate, while the temperature of the cell is monitored *in situ* in a battery testing calorimeter (BTC) (Figure 1d and S1, Supporting Information). Such programmed temperature profile simulate heat generation when a cell undergoes a hard internal-short circuit (Stage 1) (Figure 1f). As the temperature increases, the accumulated heat within the cell vaporizes the organic electrolytes (Stage 2), and eventually explosion occurs due to the over-pressure ordmeombustion (Stage 3). Such explosion will introduce a positive or negative temperature jump (TJ) in the temperature profile (Figure 1d,e) due to the heat exchange between the cell and the environment. The explosion can destroy or deform the cell and the electrodes/separator layers will be scattered within the testing chamber (Figure 1b,c). The objective of this study is to gain molecular insight into the structure derived explosion behaviours of the electrolyte in Mg-S battery.

DME, DEG and TEG are selected as the target electrolytes for the performance, safety and cost evaluation. They are linearly shaped ethers in the form of $CH_3O(CH_2CH_2O)_nCH_3$ with *n* equal to 1, 2 and 4, respectively. All of them reach the initial discharge capacity of 800 mAh g^{-1} (**Figure 2**), while the first charge capacities are 800, 717 and 328 mAh g^{-1} for DME, DEG and TEG-cells, respectively. After three cycles the specific discharge capacities of DEG and TEG-cells are 61% and 46% of DME-cell (491 mAh g^{-1}). In addition, the discharge plateaus of DME and DEG-cells are at 1.0 V while that for TEG-cell is at 0.9 V. Such a difference in specific capacity stems from the number of CH_2CH_2O groups in the molecular structure. A longer molecule leads to reduced mobility of the electrolyte and thus higher resistance towards Mg^{2+} transportation [23,40]. As a result, the Mg^{2+} diffusion towards the CMK-3/S cathode is limited, causing insufficient charging and discharging.

Firstly, the fresh cells are tested in the BTC: a steady and linear temperature increase is found for all three cells during heating (**Figure 3**a). Unlike the profile in conventional Li-ion batteries [37,41–43], here no significant heat generation is found in the form of sharp temperature spike, which suggests that combustion of Mg anode does not take place. Careful examination of all three curves reveals small TJ for DME and DEG-cells at 400 K and 450 K, respectively, indicating the explosion of the cell (Figure 3b). In comparison, no TJ is found for the TEG-cell. Indeed, the DME-cell is completely destroyed during explosion, in which all six components of the cell are all scattered in the testing chamber (Figure 3j and S2a, Supporting Information). The DEG-cell remains largely intact but with a big crack, leading to the evaporation of all the DEG electrolyte (Figure 3m and S2b, Supporting Information). The glass fibre separator layer is found to 'stretch' outside the cell. During the fast gasification, part of the glass fibre layer is carried outside the cell by the DEG electrolyte to release the over-pressure. Finally, the TEG-cell remains fully intact (Figure 3p and S2c, Supporting Information) until reaching the temperature of the testing limit (523 K).

The first derivatives of both TJs show negative peaks in the DME and DEG-cells (Figure 3c,d), indicating an endothermic process during explosion. This can be understood as the pure thermal expansion of the vaporized electrolyte during the explosion, which absorbs heat from the environment [44,45]. Therefore, the explosion of fresh DME and DEG cells is mainly a physical process due to the over-pressure caused by electrolyte vaporization and expansion.

Next, the sample explosion test is applied to the cells after three discharge and charge cycles. TJ is only recorded for the cycled-DME-cell, whereas those of the cycled-DEG-cell and cycled-TEG-cell show a steady temperature profile (Figure 3f). This is also observed in the first derivatives profiles, in which the cycled-DME-cell shows a positive peak (Figure 3g) whereas the cycled-DEG-cell present a flat line (Figure 3h). The positive peak here indicates an exothermic process for the cycled-DME-cell during explosion, which is different from its fresh state. This can be understood as the unstable decomposition reaction of the intermediate product MgS (Figure S3, Supporting Information) after cycles, which reacts as $MgS + 2H_2O \rightarrow Mg(OH)_2 + H_2S$, $\Delta H = -133.5$ kJ mol^{-1}, releasing heat. Comparison of the SEM images of cathode in the original states (Figure 3r) and the 3rd cycled state after explosion (Figure 3s, and Figure S4, Supporting Information) shows a slight aggregation of S particles. This is because of the dissolution and precipitation out of S during charging and discharging. On the anode side, no significant cracking or damage is observed in the Mg foil, except for the deposition of the glass fibres at the surface (Figure 3t,u and Figure S5, Supporting Information, which is likely due to cell disassembly). Though there were no significant fluctuations in the time-temperature curve for cycled-DEG-cell(Figure S6a-d, Supporting Information), cracks were observed after the thermal runaway test. This indicates the leak of DEG during the heating (Figure S6e, Supporting Information).

The explosion temperatures are 45 K and 20 K above the boiling points of DME and DEG (Figure 3a,e), respectively. This may be caused by a thermal resistance from the chamber environment to the inner cell. To examine this, a range of heating rates from 1 K·min^{-1} to 20

K·min^{-1} are tested. Surprisingly, the explosion temperatures for DME and DEG stay constantly at 403 ± 4 K and 455 ± 6 K, respectively, regardless of the heating rate (**Figure 4**a). The pressure of the cell is then calculated by using the vapour pressure equation and is plotted as the function of time (Figure S7, Supporting Information). The calculated vapour pressures at the explosion temperature are 249 ± 14 kPa for DME and 172 ± 28 kPa for DEG, respectively (Figure 4b). Sulfur does not contribute to the inner pressure built up, as the calculated sulfur vapour pressures at those conditions are 0.006 kPa and 0.11 kPa, respectively. Because the electrolyte vapour is the main reason for the over-pressure in the cell, the calculated vapour pressure can also reflect the real inner pressure of the cell. If decomposition of the electrolyte takes place, an additional pressure is built up. This leads to the further decrease of the thermal runaway temperature (Table S1 and Figure S8, Supporting Information). The sealing pressure of the coin cell can also influence the explosion temperature. Raising the sealing pressure from 0.5 TON to 0.75 TON increases the thermal runaway temperature from 393 K to 439 K (Figure S9, Supporting Information) for DME based electrolyte. The explosion temperature is then stabilized between 439 K and 451 K when the sealing pressure is further increased to 1.4 TONs. At 0.5 TON of the standard sealing condition, DME-cell will only explode at 149 kPa over-pressure from the environment, while the DEG-cell can explode with 72 kPa over-pressure (albeit at different failure temperatures). This indicates the upper pressure limit of the CR2032 cell at 403 K and 455 K, respectively. The Nylon-6 O-ring that seals the cells become less thermally stable above 423 K [46]. Its ability to withhold the over-pressure is then decreased. To verify this, the Nylon-6 O-ring is tested in the BTC under the same temperature programme. After test, the Nylon-6 O-ring has completely melted (Figure S10, Supporting Information). The influence of cathode sulfur loading to the explosion temperature is further studied, in order to examine if there can be any combustion of the sulfur. The result shows again the constant explosion temperature at 403 ± 4 K and 455 ± 6 K for DME and DEG-cells, respectively, regardless of the sulfur loading (Figure 4c). DME is further mixed to DEG or TEG at the volume

6

ratios of 3:1, 1:1 and 1:3, respectively, to form the mixed solvent systems. The thermal runaway temperature increases with the raising content of DEG or TEG (Figure S11a-c, Supporting Information). The overall thermal runaway temperature shows a positive correlation with the average carbon atom per molecule in the mixed electrolyte, suggesting the causal relations between molecular structure and its explosion behaviour (Figure S12, Supporting Information). The discharge/charge curves of various electrolytes show that the electrochemical performance of mixed electrolyte (DME+DEG or DME+TEG) mixture is between that of pure electrolyte systems (Figure S11d). These phenomena further confirm that thermal runaway and electrochemical performance are closely tied to the chain length of the electrolyte. We further studied Magnesium bis(hexamethyldisilazide) $Mg(HMDS)_2$ as an organic non-nucleophilic electrolyte [47–49] (Figure S13, Supporting Information). It is not soluble in DME but soluble in DEG and TEG. Similar to the thermal runaway test with $Mg(TFSI)_2$ electrolyte, a small TJ is found for DEG solvent at 438 K with 3 $K·min^{-1}$, whereas the TEG cell does not explode.

With the measured specific capacity, the explosion temperature and indicatives prices of the three electrolytes in the Acros, a comprehensive diagram can be drawn to balance the performance, cost and safety of the Mg-S batteries (**Figure 5**a). The DME-cell is clearly favoured by performance and cost, whereas the safety of DME requires serious consideration. In this regard, design of DME derivatives with higher boiling point and the same Mg^{2+} conductivity is suggested. The risk of combustion is high in DME-cells, in particular the practical pouch cells. The trends of performance, safety and cost are directly related to the number of repeating units in three $CH_3O(CH_2CH_2O)_nCH_3$ electrolytes (Figure 5b). In general, longer chain length leads to 1) high boiling point, thus high explosion temperature; 2) high Mg^{2+} conduction resistance and low storage capacity; 3) long synthetic process and high separation cost.

In conclusion, a general approach that evaluates the performance, safety and cost of the electrolyte in Mg-S battery is developed. The combustion of the metal anode is not found in the

Mg-S battery for all three electrolyte systems under the failure scenarios studied here, which provides a compelling improvement compared with other alkali metal anodes. The explosion temperature is positively correlated with the electrolyte vapour pressures and boiling points, which are the key descriptor for the safety limits of Mg-S battery. The number of the repeating unit in the electrolyte plays a decisive role in the overall battery evaluations. In general, small chain ether based electrolytes with low boiling points have a low explosion temperature. In contrast, the Mg^{2+} mobility is higher in those small chain electrolytes, leading to a better charge and discharge performance. Therefore, a potential method to realize the improvement of battery safety, while at the same time maintaining or even improving the battery performance, is to design small chain molecules with higher molecular weight or polarity, thus obtaining a higher boiling point and low vapour pressure. It is also important to study the temperature distribution within the batteries to understand the origin of the explosion. As the Mg-S technology matures, the application of these methods to larger format cells will continue to provide useful insight to benchmark its safety of compared with other cell chemistries.

Experimental section

Battery testing calorimeter: Thermal runaway testing was conducted inside a Phi-Tec Battery Testing Calorimeter (BTC) (Figure S1, Supporting Information). The coin cell is taped with the thermal couples to measure the temperature increase. The cell is placed into a protected explosion chamber. Temperature programmed heating is set at various fixed rates to reach 523 K. The temperature of the cell is measured every 5 s. After the test, the chamber is opened and the cell is examined. Each test is repeated at least three times.

Synthesis of CMK-3/S composites as cathode materials: The Mg-S battery tested in BTC uses a CMK-3/S composite as the cathode. CMK-3 is an ordered mesoporous carbon material with high surface area (1141 m^2 g^{-1}) and large pore volume (1.38 cm^3 g^{-1}) (Figure S14, Supporting Information). In a typical experiment to produce CMK-3/S composite, 0.5 g of CMK-3 powder is physically mixed with 0.5 g of sulfur. The mixture is then transferred into a

8

batch reactor under argon with subsequent heating at 428 K for 24 h. The sulfur melts and is impregnated into the pore network of CMK-3. The diffraction peaks in the X-ray diffraction pattern (XRD) are not obvious (Figure S15, Supporting Information), suggesting the formation of quasi-amorphous S. The S is indeed impregnated into the CMK-3 channels, as uniform distribution of S and C is observed in the energy-dispersive X-ray spectroscopy (Figure S16, Supporting Information).

Electrolyte preparation: Three types of electrolytes were chosen and prepared in an Ar filled glovebox by adding magnesium(II) bis(trifluoromethanesulfonyl)imide (Mg(TFSI)$_2$) into the DME, DEG and TEG, respectively. After three hours of stirring, magnesium chloride (MgCl$_2$) was added into the electrolytes and stirring overnight. The molar ratio of Mg(TFSI)$_2$ and MgCl$_2$ is 1: 0.8. The concentration of the Mg^{2+} is 1.8 mol L^{-1}.

Four types of electrolytes were prepared in an Ar filled glovebox by adding magnesium(II) bis(trifluoromethanesulfonyl)imide (Mg(TFSI)$_2$) into the pure DOL and different volume ratios of DOL:DME. The different volume ratios of DOL and DME are 1:3, 1:1, and 3:1 respectively. After three hours of stirring, magnesium chloride (MgCl$_2$) was added into the electrolytes and stirring overnight. The molar ratio of Mg(TFSI)$_2$ and MgCl$_2$ is 1: 0.8. The concentration of the Mg^{2+} is 1.8 mol L^{-1}.

Two types of electrolytes (Mg(HMDS)$_2$ system) were prepared in an Ar filled glovebox. 1.24 g (3.6 mmol) of Mg(HMDS)$_2$ was dissolved in 4 ml of DEG or TEG in a vial, then 0.96 g (7.2 mmol) of AlCl$_3$ was slowly added and stirred for 24 h at room temperature. Subsequently about 0.343 g (3.6 mmol) of MgCl$_2$, was added portionwise to the solution and stirred for 40 h.

Electrochemical measurements: All the electrochemical measurements were tested with CR2032 coin cells with magnesium foil from Goodfellow as anode, previously prepared electrolyte, Whatman glass fiber as separator and CMK-3/S cathode. This cathode was fabricated by mixing CMK-3/S composite, super P, sodium carboxyl methyl cellulose (NaCMC) and styrene butadiene rubber (SBR) in a weight ratio of 80: 10: 5: 5 in deionized water. The

slurry was coated on carbon coated aluminium foil and dried at 60 °C overnight in vacuum oven. Then, the electrode was roll pressed, and punched into round discs of 6 mm in diameter with mass loading from 0.3 to 0.6 mg_{sulfur} cm^{-2}. The volume of electrolyte is 150 µL for all the cells. Galvanostatic charge and discharge were tested in a voltage window of 0.4–1.8 V on a battery measurement system (Neware).

Characterization and thermal runaway test: XRD measurements were performed using a StadiP diffractometer from STOE, a voltage of 40 kV, at 30 mA, with Cu Kα radiation, scan in the 2θ range between 0° and 90° at a rate of 6° min^{-1} with step size of 0.5°. Nitrogen adsorption−desorption isotherms were recorded at 77 K using a Micromeritics 3Flex surface characterization analyzer. Specific surface areas were determined according to the BET model, with pore diameters, volumes, and distributions determined through the BJH method. Scanning transmission electron microscopy (STEM) study was performed using a probe corrected (CEOS) JEM ARM 200CF (JEOL, Japan) operated at 200 kV. Bright Field (BF) and High Angle Annular Dark Field (HAADF) images were acquired simultaneously. EDS elemental mapping was performed on the same microscope. Scanning electron microscopy (SEM) imaging and related element mapping were performed on a JEOL JSM-7401F SEM.

References

[1] B. Dunn, H. Kamath, J.M. Tarascon, Electrical energy storage for the grid: A battery of choices, Science. 334 (2011) 928–935. https://doi.org/10.1126/science.1212741.

[2] J.M. Tarascon, M. Armand, Issues and challenges facing rechargeable lithium batteries, Nature. 414 (2001) 359–367. https://doi.org/10.1038/35104644.

[3] J.B. Goodenough, Y. Kim, Challenges for rechargeable Li batteries, Chem. Mater. 22 (2010) 587–603. https://doi.org/10.1021/cm901452z.

[4] C. Liu, F. Li, M. Lai-Peng, H.M. Cheng, Advanced materials for energy storage, Adv. Mater. 22 (2010) E28-62. https://doi.org/10.1002/adma.200903328.

[5] H.D. Yoo, E. Markevich, G. Salitra, D. Sharon, D. Aurbach, On the challenge of developing advanced technologies for electrochemical energy storage and conversion, Mater. Today. 17 (2014) 110–121. https://doi.org/10.1016/j.mattod.2014.02.014.

[6] Y. Wang, R. Chen, T. Chen, H. Lv, G. Zhu, L. Ma, C. Wang, Z. Jin, J. Liu, Emerging non-lithium ion batteries, Energy Storage Mater. 4 (2016) 103–129. https://doi.org/10.1016/j.ensm.2016.04.001.

[7] F. Wu, G. Yushin, Conversion cathodes for rechargeable lithium and lithium-ion batteries, Energy Environ. Sci. 10 (2017) 435–459. https://doi.org/10.1039/c6ee02326f.

[8] N.S. Choi, Z. Chen, S.A. Freunberger, X. Ji, Y.K. Sun, K. Amine, G. Yushin, L.F. Nazar, J. Cho, P.G. Bruce, Challenges facing lithium batteries and electrical double-layer capacitors, Angew. Chemie - Int. Ed. 51 (2012) 9994–10024. https://doi.org/10.1002/anie.201201429.

[9] A. Manthiram, Materials challenges and opportunities of lithium ion batteries, J. Phys. Chem. Lett. 2 (2011) 176–184. https://doi.org/10.1021/jz1015422.

[10] X. Hong, J. Mei, L. Wen, Y. Tong, A.J. Vasileff, L. Wang, J. Liang, Z. Sun, S.X. Dou, Nonlithium Metal–Sulfur Batteries: Steps Toward a Leap, Adv. Mater. 31 (2019) e1802822. https://doi.org/10.1002/adma.201802822.

[11] R. Mohtadi, F. Mizuno, Magnesium batteries: Current state of the art, issues and future perspectives, Beilstein J. Nanotechnol. 5 (2014) 1291–1311. https://doi.org/10.3762/bjnano.5.143.

[12] C.B. Bucur, T. Gregory, A.G. Oliver, J. Muldoon, Confession of a Magnesium Battery, J. Phys. Chem. Lett. 6 (2015) 3578–3591. https://doi.org/10.1021/acs.jpclett.5b01219.

[13] X. Zhou, J. Tian, J. Hu, C. Li, High Rate Magnesium–Sulfur Battery with Improved Cyclability Based on Metal–Organic Framework Derivative Carbon Host, Adv. Mater. 30 (2018) 1704166. https://doi.org/10.1002/adma.201704166.

[14] S.Y. Ha, Y.W. Lee, S.W. Woo, B. Koo, J.S. Kim, J. Cho, K.T. Lee, N.S. Choi, Magnesium(II) bis(trifluoromethane sulfonyl) imide-based electrolytes with wide electrochemical windows for rechargeable magnesium batteries, ACS Appl. Mater. Interfaces. 6 (2014) 4063–4073. https://doi.org/10.1021/am405619v.

[15] X.C. Hu, Y. Shi, S.Y. Lang, X. Zhang, L. Gu, Y.G. Guo, R. Wen, L.J. Wan, Direct insights into the electrochemical processes at anode/electrolyte interfaces in magnesium-sulfur batteries, Nano Energy. 49 (2018) 453–459. https://doi.org/10.1016/j.nanoen.2018.04.066.

[16] Y. Xu, W. Li, G. Zhou, Z. Pan, Y. Zhang, A non-nucleophilic mono-Mg^{2+} electrolyte for rechargeable Mg/S battery, Energy Storage Mater. 14 (2018) 253–257. https://doi.org/10.1016/j.ensm.2018.03.020.

[17] R. Davidson, A. Verma, D. Santos, F. Hao, C. Fincher, S. Xiang, J. Van Buskirk, K. Xie, M. Pharr, P.P. Mukherjee, S. Banerjee, Formation of Magnesium Dendrites during Electrodeposition, ACS Energy Lett. 4 (2019) 375–376. https://doi.org/10.1021/acsenergylett.8b02470.

[18] P. Wang, M.R. Buchmeiser, Rechargeable Magnesium–Sulfur Battery Technology: State of the Art and Key Challenges, Adv. Funct. Mater. 29 (2019) 1905248. https://doi.org/10.1002/adfm.201905248.

[19] P. Saha, P.H. Jampani, D.H. Hong, B. Gattu, J.A. Poston, A. Manivannan, M.K. Datta, P.N. Kumta, Synthesis and electrochemical study of $Mg_{1.5}MnO_3$: A defect spinel cathode for rechargeable magnesium battery, Mater. Sci. Eng. B Solid-State Mater. Adv. Technol. 202 (2015) 8–14. https://doi.org/10.1016/j.mseb.2015.08.008.

[20] L. Kong, C. Yan, J.-Q. Huang, M.-Q. Zhao, M.-M. Titirici, R. Xiang, Q. Zhang, A Review of Advanced Energy Materials for Magnesium-Sulfur Batteries, Energy Environ. Mater. 1 (2018) 100–112. https://doi.org/10.1002/eem2.12012.

[21] Z. Zhao-Karger, M. Fichtner, Magnesium-sulfur battery: Its beginning and recent progress, MRS Commun. 7 (2017) 770–784. https://doi.org/10.1557/mrc.2017.101.

[22] S.H. Chung, A. Manthiram, Current Status and Future Prospects of Metal–Sulfur Batteries, Adv. Mater. 31 (2019) e1901125. https://doi.org/10.1002/adma.201901125.

[23] Z. Zhao-Karger, M.E. Gil Bardaji, O. Fuhr, M. Fichtner, A new class of non-corrosive, highly efficient electrolytes for rechargeable magnesium batteries, J. Mater. Chem. A. 5 (2017) 10815–10820. https://doi.org/10.1039/c7ta02237a.

[24] T. Gao, M. Noked, A.J. Pearse, E. Gillette, X. Fan, Y. Zhu, C. Luo, L. Suo, M.A. Schroeder, K. Xu, S.B. Lee, G.W. Rubloff, C. Wang, Enhancing the Reversibility of Mg/S Battery Chemistry through Li^+ Mediation, J. Am. Chem. Soc. 137 (2015) 12388–12393. https://doi.org/10.1021/jacs.5b07820.

[25] B.P. Vinayan, Z. Zhao-Karger, T. Diemant, V.S.K. Chakravadhanula, N.I. Schwarzburger, M.A. Cambaz, R.J. Behm, C. Kübel, M. Fichtner, Performance study of magnesium-sulfur battery using a graphene based sulfur composite cathode electrode and a non-nucleophilic Mg electrolyte, Nanoscale. 8 (2016) 3296–3306. https://doi.org/10.1039/c5nr04383b.

[26] T. Gao, S. Hou, F. Wang, Z. Ma, X. Li, K. Xu, C. Wang, Reversible S^0/MgS$_x$ Redox Chemistry in a MgTFSI$_2$/MgCl$_2$/DME Electrolyte for Rechargeable Mg/S Batteries, Angew. Chemie - Int. Ed. 56 (2017) 13526–13530. https://doi.org/10.1002/anie.201708241.

[27] K. Kitoh, H. Nemoto, 100 Wh large size Li-ion batteries and safety tests, J. Power Sources. 81–82 (1999) 887–890. https://doi.org/10.1016/S0378-7753(99)00125-1.

[28] R. Kizilel, R. Sabbah, J.R. Selman, S. Al-Hallaj, An alternative cooling system to enhance the safety of Li-ion battery packs, J. Power Sources. 194 (2009) 1105–1112. https://doi.org/10.1016/j.jpowsour.2009.06.074.

[29] D. Doughty, E.P. Roth, A general discussion of Li Ion battery safety, Electrochem. Soc. Interface. 21 (2012) 37–44. https://doi.org/10.1149/2.F03122if.

[30] E.P. Roth, C.J. Orendorff, How electrolytes influence battery safety, Electrochem. Soc. Interface. 21 (2012) 45–49. https://doi.org/10.1149/2.F04122if.

[31] K. Liu, Y. Liu, D. Lin, A. Pei, Y. Cui, Materials for lithium-ion battery safety, Sci. Adv. 4 (2018) eaas9820. https://doi.org/10.1126/sciadv.aas9820.

[32] D.P. Finegan, J. Darst, W. Walker, Q. Li, C. Yang, R. Jervis, T.M.M. Heenan, J. Hack, J.C. Thomas, A. Rack, D.J.L. Brett, P.R. Shearing, M. Keyser, E. Darcy, Modelling and experiments to identify high-risk failure scenarios for testing the safety of lithium-ion cells, J. Power Sources. 417 (2019) 29–41. https://doi.org/10.1016/j.jpowsour.2019.01.077.

[33] Q. Wang, L. Jiang, Y. Yu, J. Sun, Progress of enhancing the safety of lithium ion battery from the electrolyte aspect, Nano Energy. 55 (2019) 93–114. https://doi.org/10.1016/j.nanoen.2018.10.035.

[34] G. Zhang, L. Cao, S. Ge, C.Y. Wang, C.E. Shaffer, C.D. Rahn, Reaction temperature sensing (RTS)-based control for Li-ion battery safety, Sci. Rep. 5 (2015) 18237. https://doi.org/10.1038/srep18237.

[35] R. Chen, A.M. Nolan, J. Lu, J. Wang, X. Yu, Y. Mo, L. Chen, X. Huang, H. Li, The Thermal Stability of Lithium Solid Electrolytes with Metallic Lithium, Joule. 4 (2020) 812–821. https://doi.org/10.1016/j.joule.2020.03.012.

[36] T.M. Bandhauer, S. Garimella, T.F. Fuller, A Critical Review of Thermal Issues in Lithium-Ion Batteries, J. Electrochem. Soc. 158 (2011) R1. https://doi.org/10.1149/1.3515880.

[37] Q. Wang, P. Ping, X. Zhao, G. Chu, J. Sun, C. Chen, Thermal runaway caused fire and explosion of lithium ion battery, J. Power Sources. 208 (2012) 210–224. https://doi.org/10.1016/j.jpowsour.2012.02.038.

[38] J. Duan, X. Tang, H. Dai, Y. Yang, W. Wu, X. Wei, Y. Huang, Building Safe Lithium-Ion Batteries for Electric Vehicles: A Review, Electrochem. Energy Rev. 3 (2020) 1–42. https://doi.org/10.1007/s41918-019-00060-4.

[39] G. Xu, L. Huang, C. Lu, X. Zhou, G. Cui, Revealing the multilevel thermal safety of lithium batteries, Energy Storage Mater. 31 (2020) 72–86. https://doi.org/10.1016/j.ensm.2020.06.004.

[40] L. Carbone, M. Gobet, J. Peng, M. Devany, B. Scrosati, S. Greenbaum, J. Hassoun, Comparative Study of Ether-Based Electrolytes for Application in Lithium-Sulfur Battery, ACS Appl. Mater. Interfaces. 7 (2015) 13859–13865. https://doi.org/10.1021/acsami.5b02160.

[41] X. Feng, J. Sun, M. Ouyang, F. Wang, X. He, L. Lu, H. Peng, Characterization of penetration induced thermal runaway propagation process within a large format lithium ion battery module, J. Power Sources. 275 (2015) 261–273. https://doi.org/10.1016/j.jpowsour.2014.11.017.

[42] A.W. Golubkov, D. Fuchs, J. Wagner, H. Wiltsche, C. Stangl, G. Fauler, G. Voitic, A. Thaler, V. Hacker, Thermal-runaway experiments on consumer Li-ion batteries with metal-

oxide and olivin-type cathodes, RSC Adv. 4 (2014) 3633–3642. https://doi.org/10.1039/c3ra45748f.

[43] S. Wilke, B. Schweitzer, S. Khateeb, S. Al-Hallaj, Preventing thermal runaway propagation in lithium ion battery packs using a phase change composite material: An experimental study, J. Power Sources. 340 (2017) 51–59. https://doi.org/10.1016/j.jpowsour.2016.11.018.

[44] X. Ge, X. Wang, Estimation of freezing point depression, boiling point elevation, and vaporization enthalpies of electrolyte solutions, Ind. Eng. Chem. Res. 48 (2009) 2229–2235. https://doi.org/10.1021/ie801348c.

[45] V.S. Patwardhan, A. Kumar, A unified approach for prediction of thermodynamic properties of aqueous mixed-electrolyte solutions. Part I: Vapor pressure and heat of vaporization, AIChE J. 32 (1986) 1419–1428. https://doi.org/10.1002/aic.690320903.

[46] G. Rusu, E. Rusu, Evaluation of thermal and dielectric behaviour of some anionic nylon 612 copolymers, Mater. Des. 31 (2010) 4601–4610. https://doi.org/10.1016/j.matdes.2010.05.042.

[47] Z. Zhao-Karger, X. Zhao, D. Wang, T. Diemant, R.J. Behm, M. Fichtner, Performance improvement of magnesium sulfur batteries with modified non-nucleophilic electrolytes, Adv. Energy Mater. 5 (2015) 1401155. https://doi.org/10.1002/aenm.201401155.

[48] A. Du, Z. Zhang, H. Qu, Z. Cui, L. Qiao, L. Wang, J. Chai, T. Lu, S. Dong, T. Dong, H. Xu, X. Zhou, G. Cui, An efficient organic magnesium borate-based electrolyte with non-nucleophilic characteristics for magnesium-sulfur battery, Energy Environ. Sci. 10 (2017) 2616–2625. https://doi.org/10.1039/c7ee02304a.

[49] D. Huang, S. Tan, M. Li, D. Wang, C. Han, Q. An, L. Mai, Highly Efficient Non-Nucleophilic $Mg(CF_3SO_3)_2$-Based Electrolyte for High-Power Mg/S Battery, ACS Appl. Mater. Interfaces. 12 (2020) 17474–17480. https://doi.org/10.1021/acsami.0c00196.
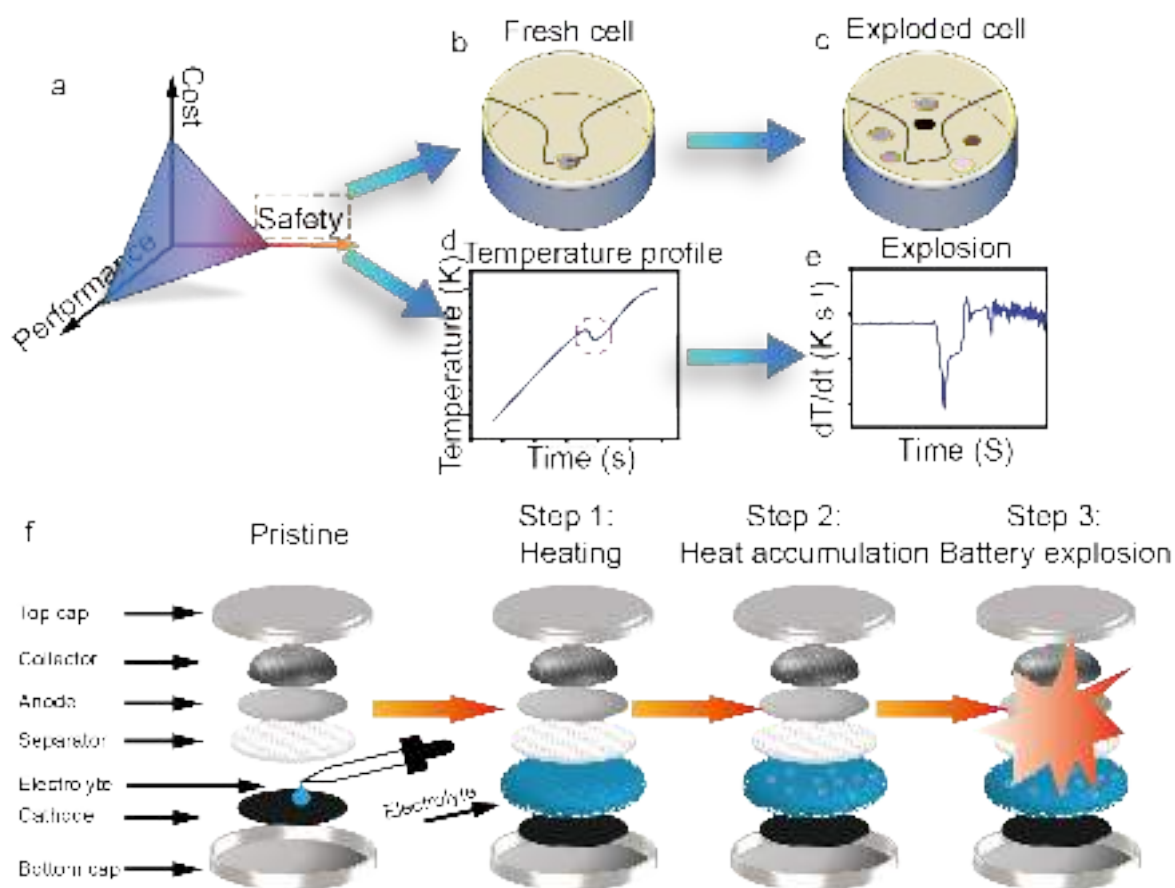
Figure 1. (a) Three criteria for battery evaluation. (b, c) Schematic diagram before and after coin cells thermal runaway test. (d) Coin cells temperature change during thermal runaway test and (e) the first-order derivative of (d). (f) Schematic of three battery stages in the explosion test.
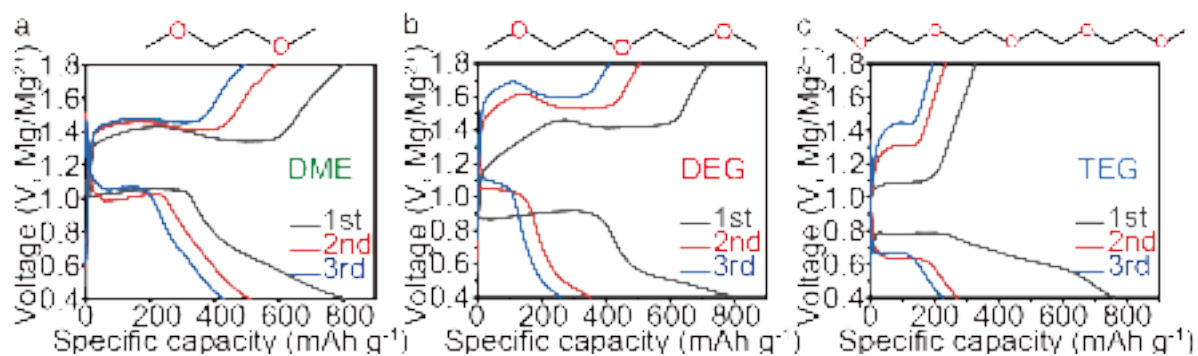

Figure 2. (a, b, c) Charge and discharge curve of DME cell, DEG cell and TEG cell respectively.
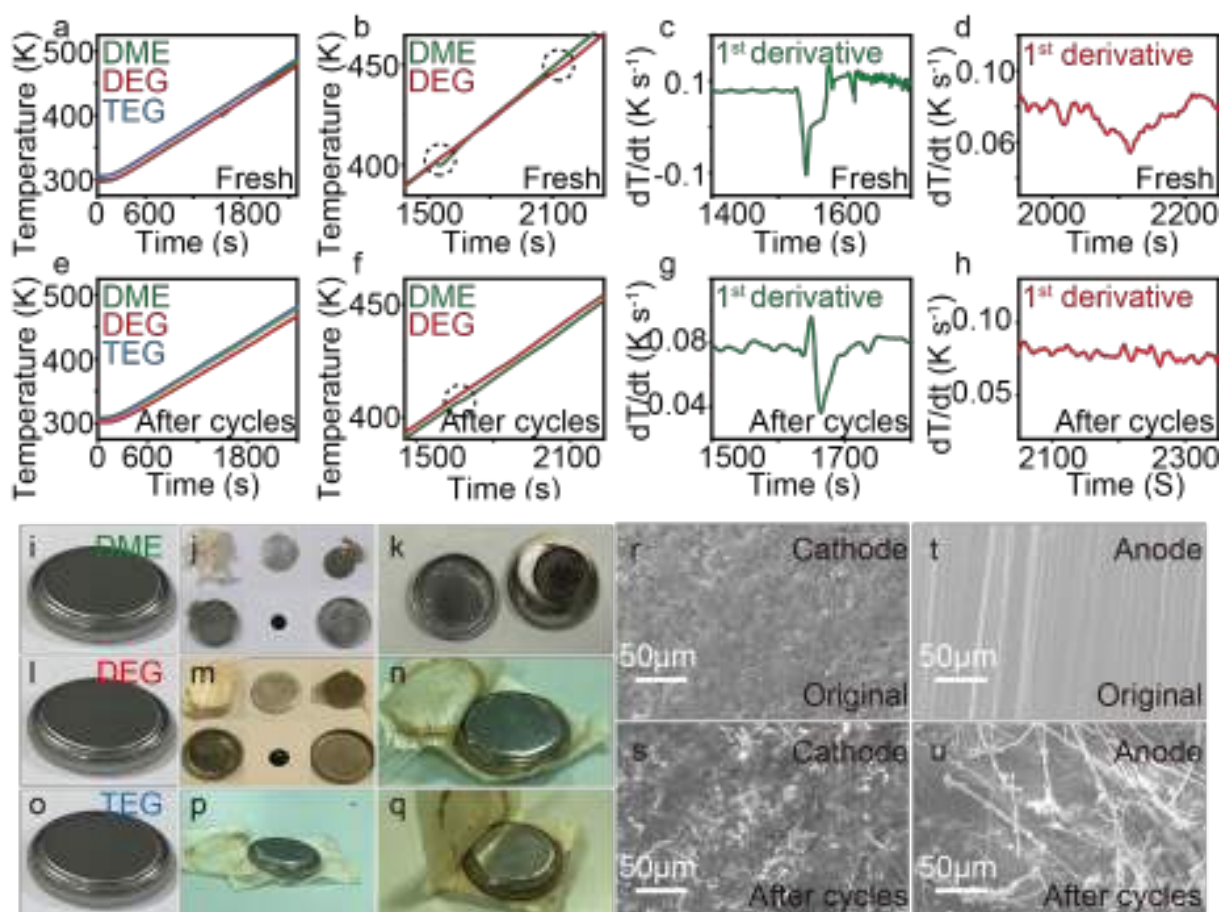
Figure 3. (a,e) Temperature profile during the simulated thermal runaway test for fresh and cycled cells DME (green), DEG (red) and TEG (blue). (b,f) are enlarged views of (a,e). The heating rate is 5 K·min^{-1}. (c,d), (g,h) First derivatives of the TJs for (c,g) DME-cells and (d,h) DEG-cells. (i-q) Digital photo of the DME, DEG and TEG cell before (i,l,o), fresh cells after simulated thermal runaway test (j,m,p) and after cycles cells after simulated thermal runaway test (k,n,q), respectively. (j,m) The six components after the test are presented in the order of glass fibre, Mg foil, Ni foam, top cap, cathode, bottom cap. Scanning electron microscopy images of the original states (Figure 3r,t) and the 3rd cycled state after explosion (Figure 3s,u).
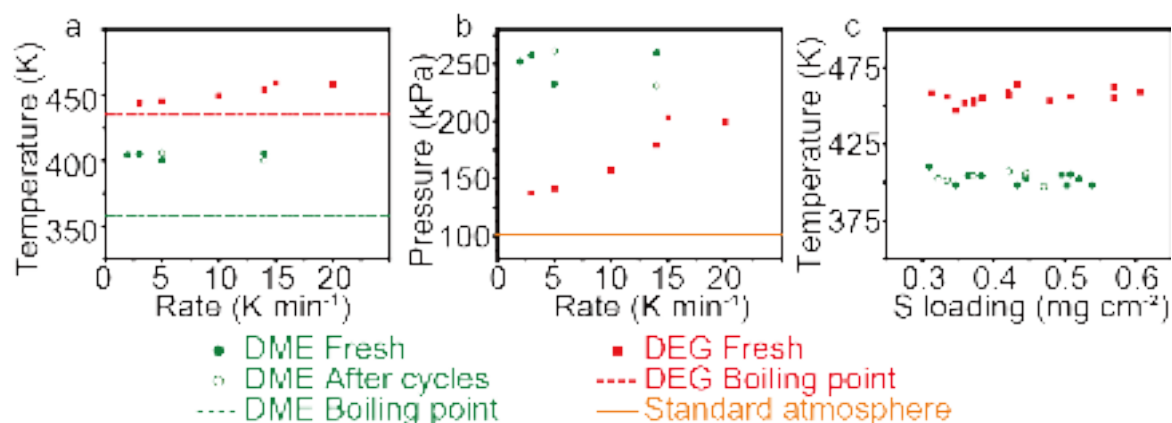
Figure 4. (a) Explosion temperature as a function of heating rates for DME (green) and DEG-cells (red). (b) The corresponding vapour pressure at the explosion temperature. (c) Explosion temperature as the function of the sulfur loading for DME (green) and DEG-cells (red). The TEG cells does not explode due to the high boiling point of TEG.
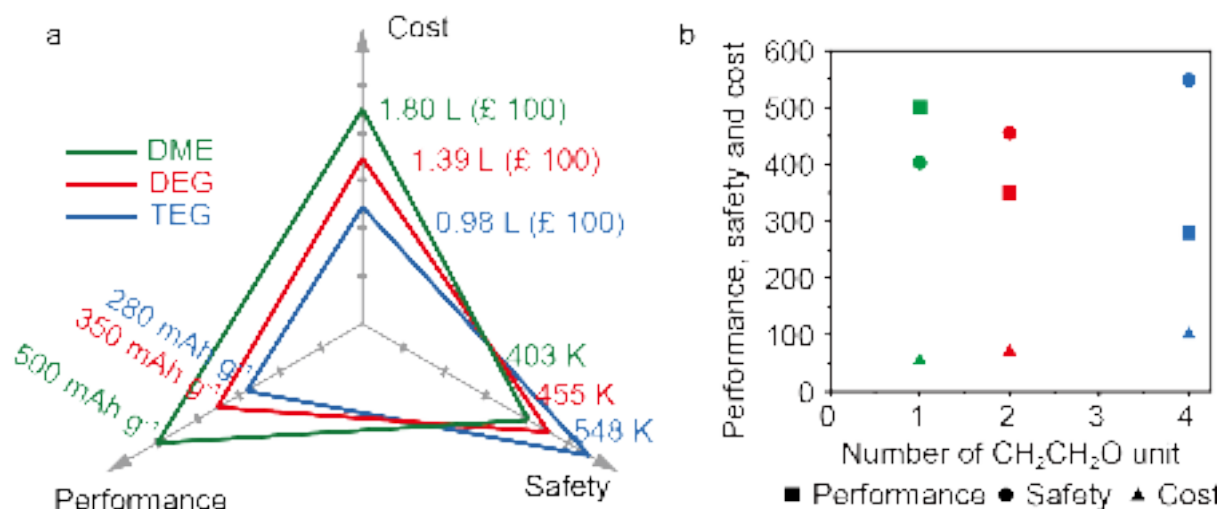
Figure 5. (a) The discharge capacity (Performance), and the explosion temperature for DME (green), DEG (red) and TEG-cells (blue), and the quantity of electrolyte with the value £ 100. The explosion temperature of the DME and DEG cells are taken from the average values in Figure 4. The explosion temperature of the TEG cell is estimated to be its boiling point. (b) The discharge capacity (mAh·g^{-1}), explosion temperature (K) and listed price at Acros (£) per one litre as the function of n in $CH_3O(CH_2CH_2O)_nCH_3$.

The safety of the MgS battery is mainly related to the vapour pressure of the electrolyte. The over-pressure builds up along with heating of the cell and triggers the battery explosion. The subsequent exothermic reaction between MgS and H_2O caused a sudden temperature jump of the battery. A modified DME with higher boiling point will be ideal of the MgS battery.

Keywords: magnesium-sulfur battery, electrolyte, safety, vapour pressure, thermal runaway

Lin Sheng, Zhangxiang Hao, Junrun Feng, Wenjia Du, Manxi Gong, Liqun Kang, Paul R. Shearing, Dan J. L. Brett, Yunhui Huang,* Feng Ryan Wang*

Evaluation and Realization of Safer Mg-S Battery: the Decisive Role of the Electrolyte

TOC
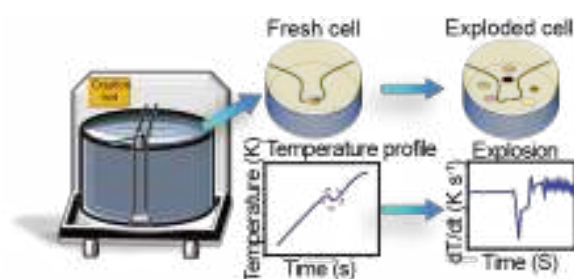
Supporting Information

Evaluation and Realization of Safer Mg-S Battery: the Decisive Role of the Electrolyte

Lin Sheng[‡a], Zhangxiang Hao[‡a], Junrun Feng[a], Wenjia Du[c], Manxi Gong[a], Liqun Kang[a], Paul R. Shearing[c,d], Dan J. L. Brett[c], Yunhui Huang,[b,*] Feng Ryan Wang[a,*]
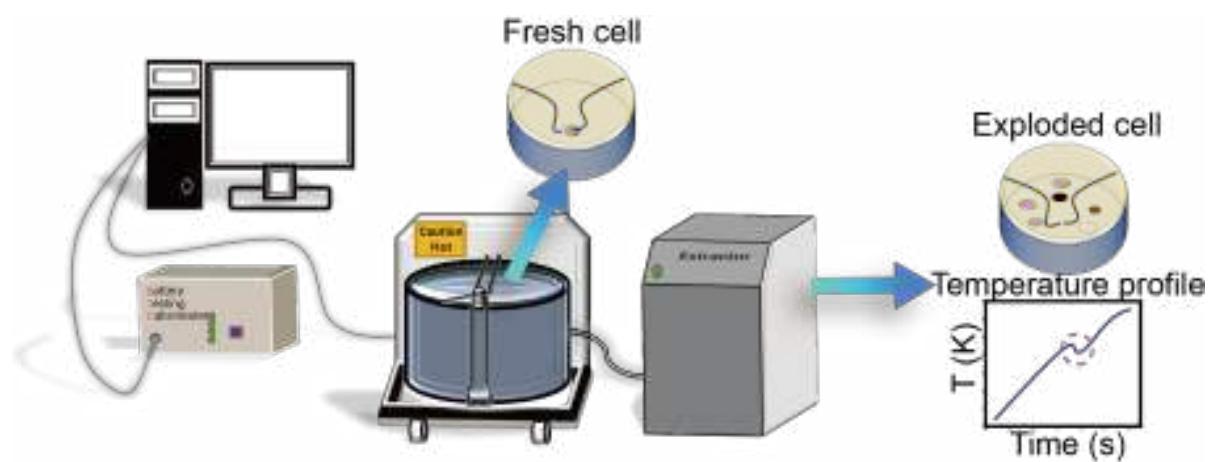
Figure S1. Schematic of the device diagrams for the battery testing calorimeter.
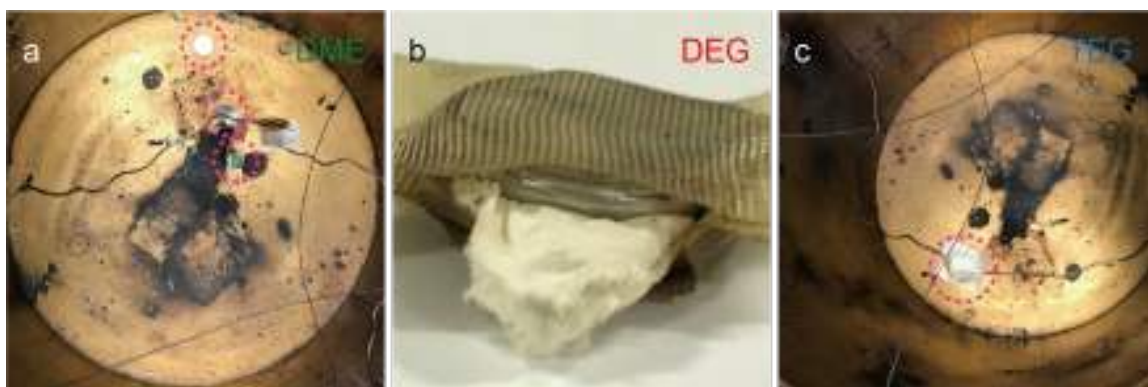
Figure S2. Digital images of the cell after explosion a) fresh-DME-cell; b) fresh-DEG-cell; c) fresh-TEG-cell.
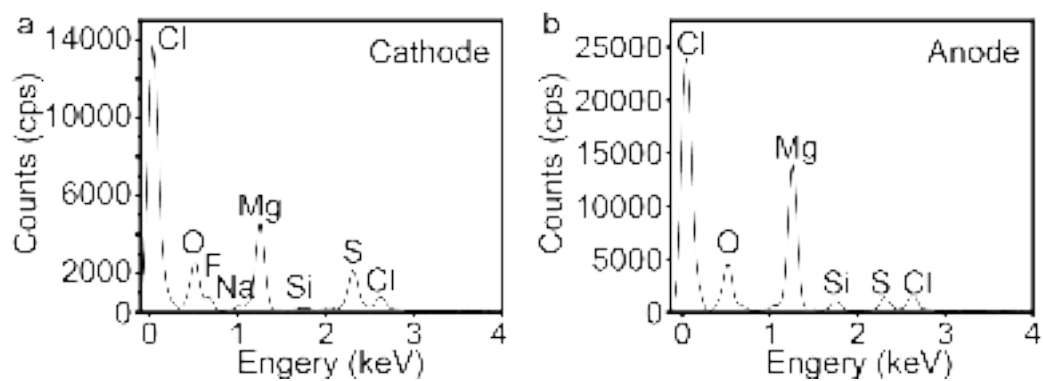
Figure S3. Energy-dispersive X-ray spectroscopy of cathode (a) and anode (b) the 3rd cycled

state after explosion in DME cell.
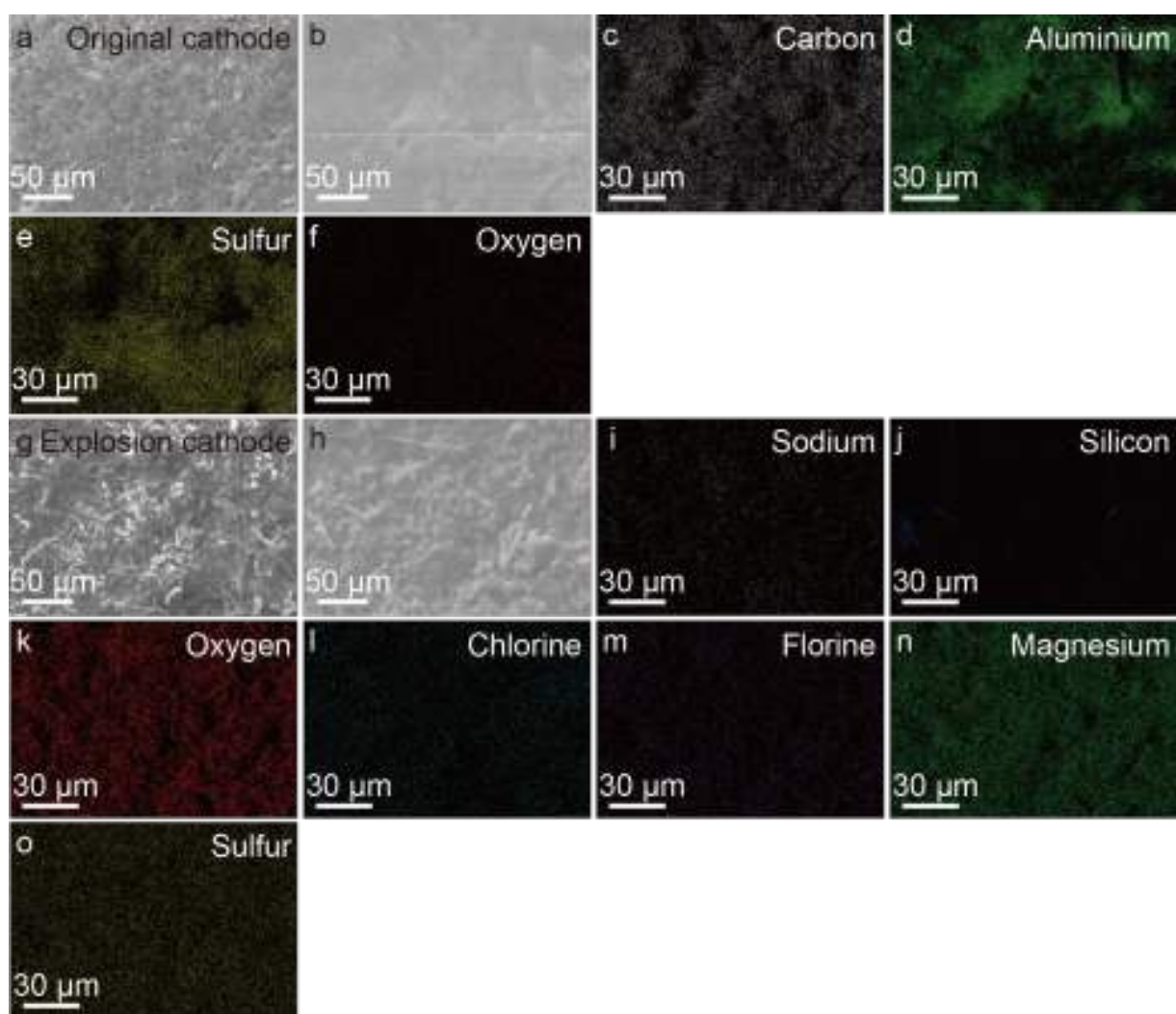
**Figure S4.** Cathode EDS mapping of original (a-f) and the 3rd cycled state after explosion (g-o) in DME cell.
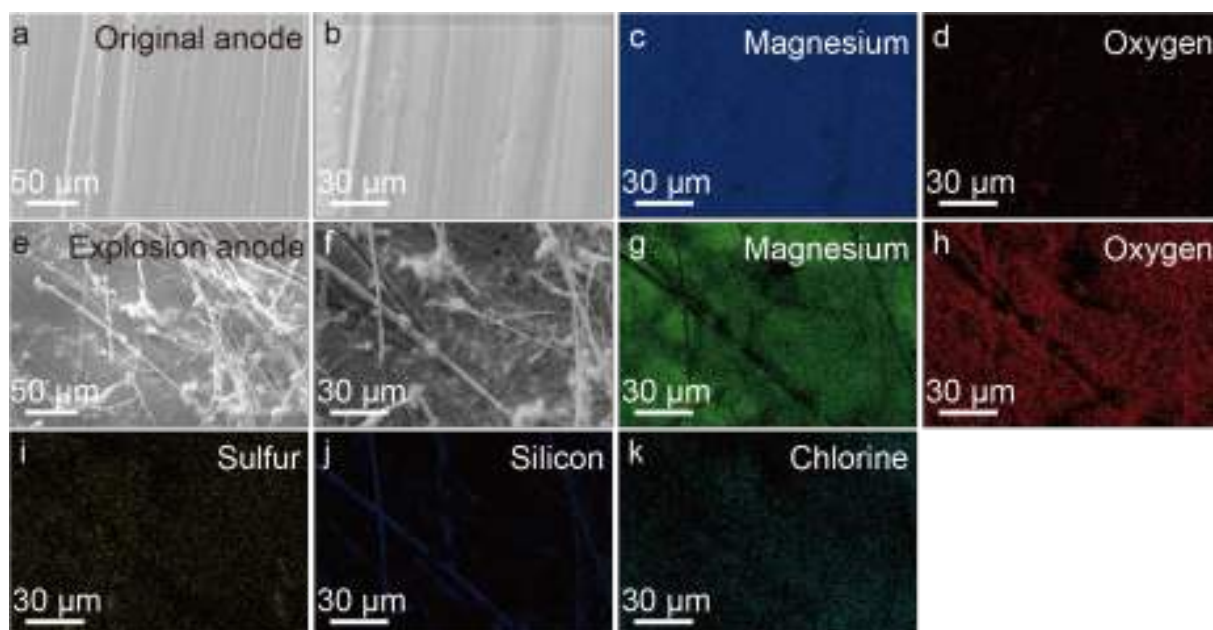
Figure S5. Anode EDS mapping of original (a-d) and the 3rd cycled state after explosion (e-k) in DME cell.
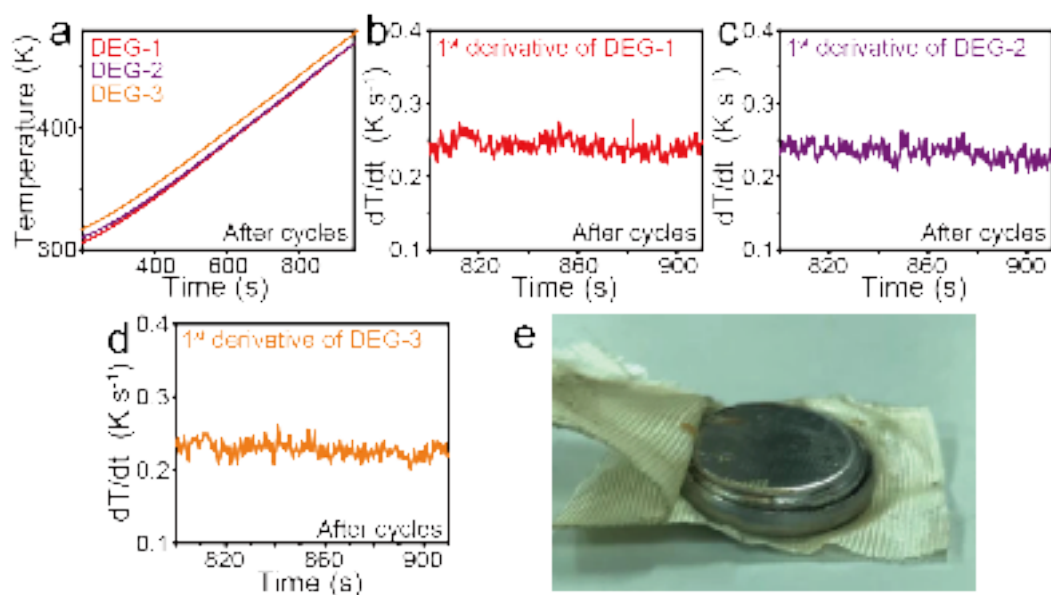
Figure S6. (a) Temperature profile during the simulated thermal runaway test for three samples of cycled DEG cells. First derivatives of the TJs for DEG cell sample 1 (b), sample 2 (c) and sample 3 (d). (e) Digital photo of after cycles DEG cell after simulated thermal runaway test.
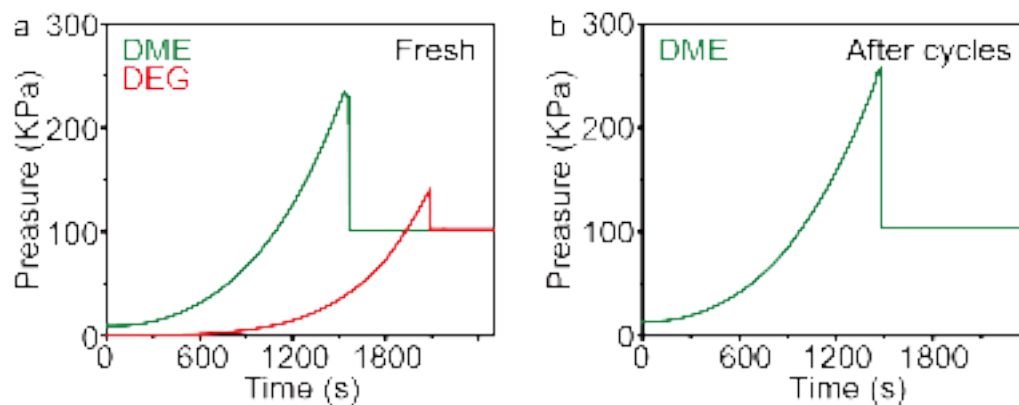
Figure S7. The pressure of the cell as the function of the heating time. The pressure is calculated from the vapour pressure equation (from National Institute of Standards and Technology) before explosion. After explosion, the measured pressure of the whole testing champ is presented.
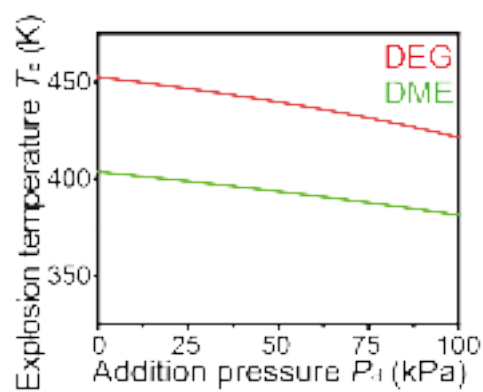
Figure S8. The function graph of T_e (explosion temperature) and P_d (addition pressure) from the decomposition of the electrolyte. The explicit equations of T_e and P_d are shown in supporting information titled "calculated equation of the vapour pressure and temperature".
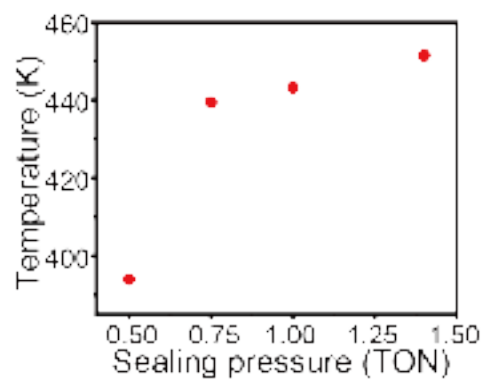
Figure S9. Explosion temperature as a function of sealing pressure for DME.
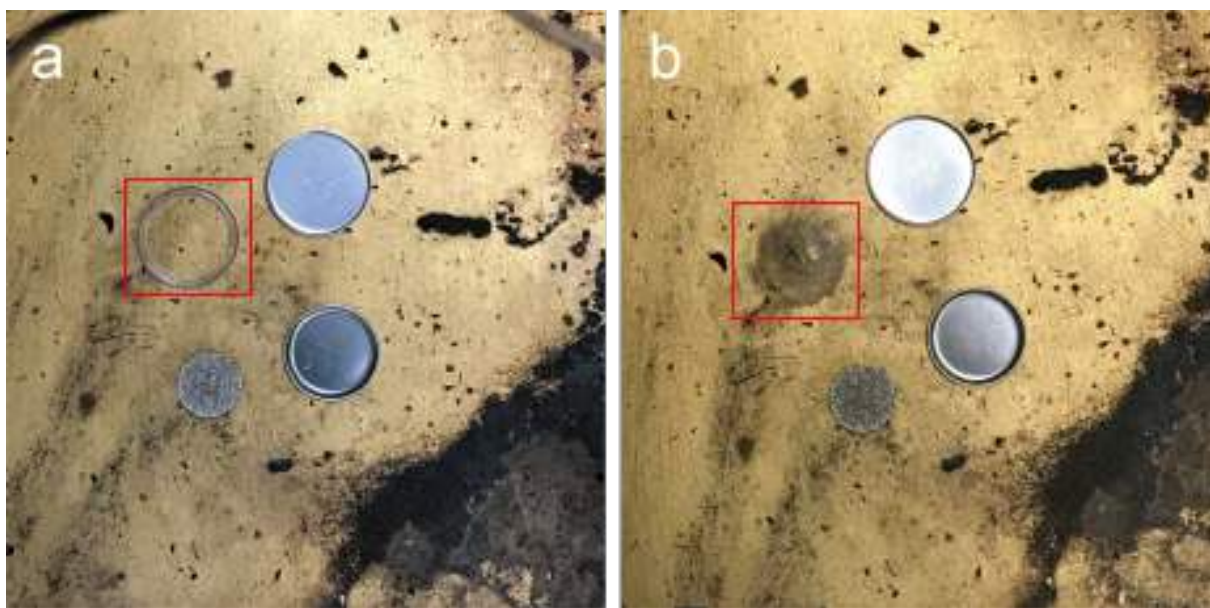
**Figure S10.** Digital photos about before and after heating test of Nylon-6 O-ring.
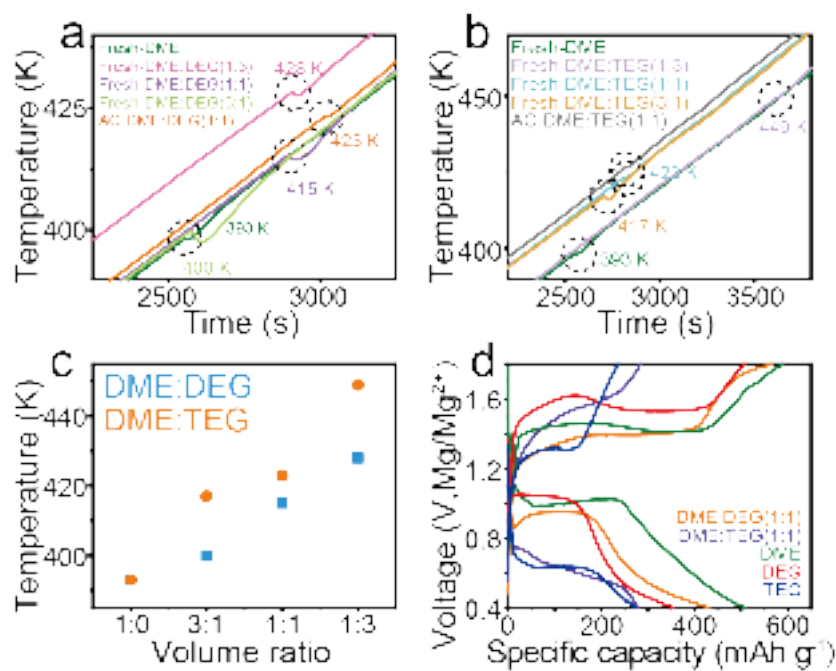
Figure S11. Temperature profile during the simulated thermal runaway test for fresh and cycled cells of DME to DEG (a), TEG (b) in different volume ratio. The heating rate is at 3 K/min. (c) Scatter plots of DME:DEG and DME:TEG at different volume ratios. (d) The 2nd cycle of charge and discharge curve of DME-DEG(1:1) and DME-TEG(1:1) cells.
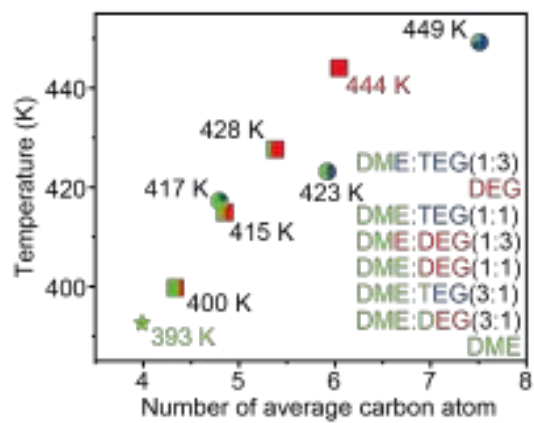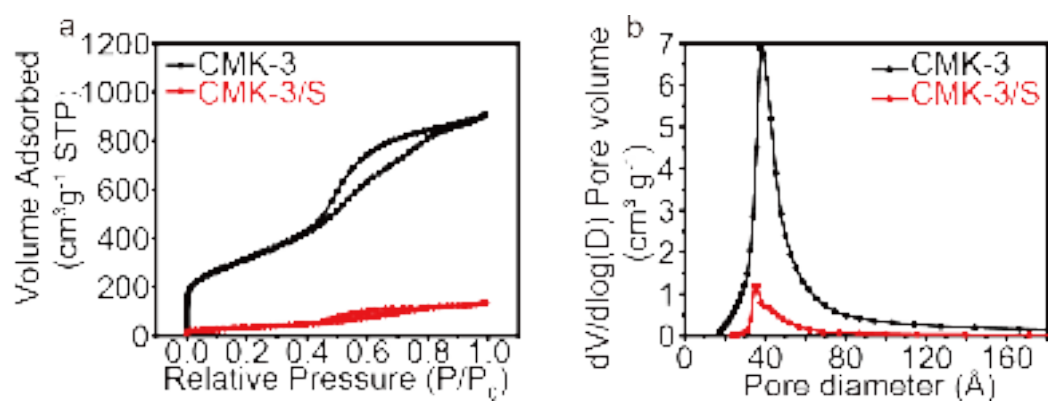
Figure S12. Scatter plots of correlation between thermal runaway temperature and number of average carbon atom per molecule.
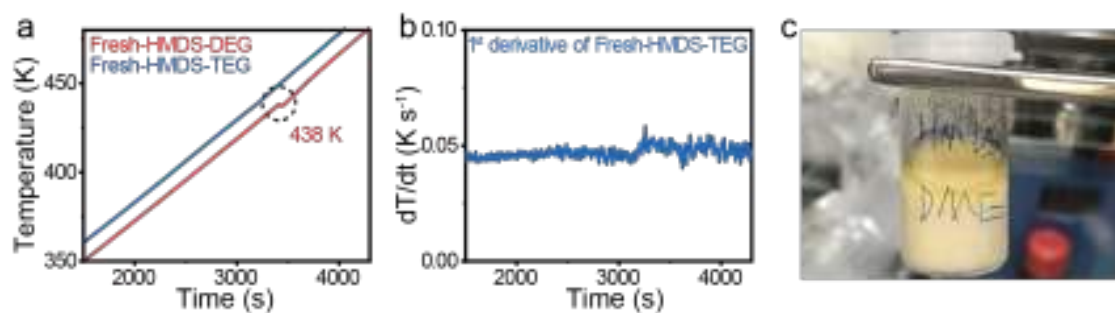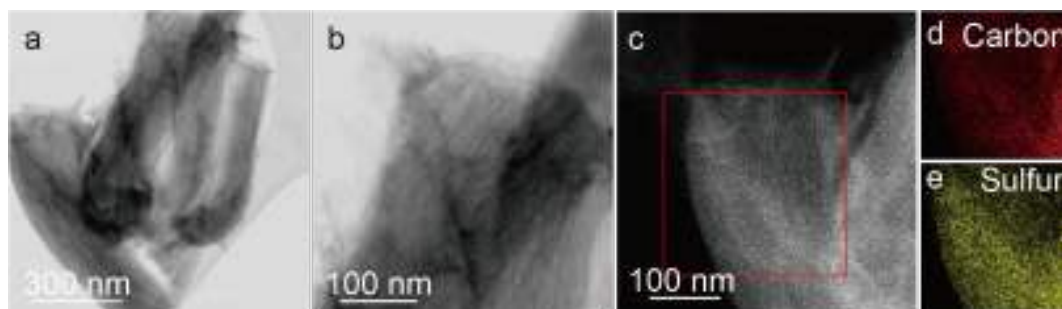
Figure S13. (a) Temperature profile during the simulated thermal runaway test for fresh cells of HMDS-DEG and HMDS-TEG. (b) First derivatives of the TJs for Fresh-HDMS-TEG cell. (c) Digital photo of HMDS-DME.

Figure S14. N_2-physisorption isotherms (a) and pore size distribution (b) of CMK-3 (black) and CMK-3/S (red).
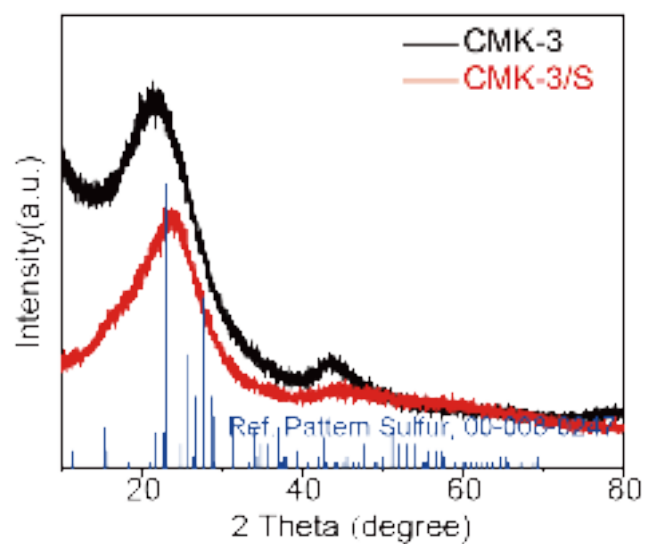
Figure S15. X-ray diffraction patterns of CMK-3 and CMK-3/S.

Figure S16. (a,b) Bright field-scanning transmission electron microscopy images of CMK-3/S. (c) High angle annular dark field-scanning transmission electron microscopy image. Element mapping of carbon (d) and sulfur (e) within the selected region of (c).

Calculated equation of the vapour pressure and temperature.

Inner pressure can be calculated based on the vapour pressure of the electrolyte. Along with the heating programme, the inner pressure that is gained from vaporization of the electrolyte is determined as the function of temperature:

$$\mathbf{log_{10}(P) = A - \frac{B}{T+C}}[1,2]$$

Where, P_I = vapour pressure (bar), T = temperature (K) and the values of A, B, and C for DME and DEG are listed in Table S1.

If the electrolyte decomposes, an addition pressure P_d is built up and this will reduce the explosion temperature (T_e), which can by calculated by:

$$\log_{10}(P_I - P_d) = A - \frac{B}{T_e + C}$$

So,

$$T_e = \frac{B}{A - \log_{10}(P_I - P_d)} - C$$

The function graph in Figure SX of T_e (explosion temperature) and P_d (addition pressure) from the decomposition of the electrolyte is based on this equation.

Table S1. Vapor pressure equation parameters [1,2]

	Suitable Temperature range (K)	A	B	C
DME	225 - 366	3.83775	1260.52	-37.322
DEG	286 - 433	4.87223	1922.137	-38.063

References

[1] D.R. Stull, Vapor Pressure of Pure Substances. Organic and Inorganic Compounds, Ind. Eng. Chem. 39 (1947) 517–540. https://doi.org/10.1021/ie50448a022.

[2] J.A. Dean, N.A. Lange, Lange's Handbook of Chemistry, McGraw-Hill, 1992.